Laminar Separation Bubble Development on a Finite Wing

Connor E. Toppings,* John W. Kurelek,† and Serhiy Yarusevych‡
University of Waterloo, Waterloo Ontario N2L 3G1, Canada

https://doi.org/10.2514/1.J060258

This experimental study considers the development of a laminar separation bubble formed over a finite wing and contrasts it with the flow evolution over a two-dimensional airfoil. The experiments were performed on a reference NACA 0018 airfoil model and a finite wing with an aspect ratio of 2.5 at a Reynolds number of 125,000 involving surface pressure and particle image velocimetry measurements. For equivalent effective angles of attack, the results reveal significant differences between the two- and three-dimensional configurations. Specifically, increasing the effective angle of attack causes the separation bubble to shift upstream on the two-dimensional airfoil, whereas its mean position and streamwise extent remain invariant to spanwise changes in the effective angle on the finite wing. Similarly, the dominant shear layer frequency and characteristics of shear layer rollers do not vary appreciably over the wingspan. This suggests that the sectional analogy between the local effective angle on the wing and that on the airfoil is not universally applicable to the wing sections subjected to the formation of laminar separation bubbles. Instead, the spanwise characteristics of the bubble on the wing are well approximated by those obtained on the airfoil at the angle of attack matching the effective angle of the wing root. It should be noted, however, that these findings are exclusive of the regions in the immediate vicinity of the wing tip and/or root, which were not considered in the present investigations.

Nomenclature

AR	=	aspect ratio
C_l	=	sectional lift coefficient; $l/(Q_\infty c)$
$C_{\overline{p}}$	=	coefficient of mean surface pressure; $(\overline{p} - P_\infty)/Q_\infty$
c	=	airfoil chord length, m
f	=	frequency, Hz
f_0	=	central instability frequency, Hz
l	=	sectional lift force, $\mathrm{N/m^{-1}}$
P_∞	=	freestream static pressure, Pa
p	=	pressure, Pa
Q_∞	=	freestream dynamic pressure; $(1/2)\rho U_\infty^2$, Pa
Re_c	=	chord-based Reynolds number; $U_\infty c/\nu$
St	=	Strouhal number; fc/U_∞
St_0	=	Strouhal number based on central instability frequency; $f_0 c/U_\infty$
s	=	wing semispan, m
t	=	time, s
U_∞	=	freestream velocity, $\mathrm{m \cdot s^{-1}}$
u, v, w	=	wall-tangent, wall-normal, and spanwise velocity components in surface attached coordinates, $\mathrm{m \cdot s^{-1}}$
X, Z	=	chordwise and spanwise coordinates, m
x, y	=	wall-tangent and wall-normal surface attached coordinates, m
x_r	=	x location of reattachment, m
x_s	=	x location of separation, m
x_t	=	x location of transition, m
α	=	angle of attack
α_{eff}	=	effective angle of attack
Δt	=	time interval, s
$\Delta_1, \Delta_2, \Delta_3$	=	difference between local pressure coefficients on wing and airfoil
μ_i	=	lifting line parameter; $c(\partial C_l/\partial\alpha)/(8s)$
ν	=	kinematic viscosity, $\mathrm{m^2 \cdot s^{-1}}$
$\Phi_{v'v'}$	=	normalized power spectral density of surface-normal velocity fluctuations
ϕ_i	=	angular spanwise coordinate, rad
ω	=	vorticity, $\mathrm{s^{-1}}$

Subscript

a_{RMS}	=	root mean square of a

Superscripts

$\overline{a}$	=	time average of a
a'	=	fluctuating component of a

I. Introduction

LAMINAR boundary-layer separation is a common occurrence for airfoils operating in the low-Reynolds-number regime ($Re_c \lessapprox 5 \times 10^5$) and can detrimentally affect performance [1,2]. If the laminar boundary layer on the suction side of an airfoil separates, the formed laminar shear layer undergoes turbulent transition and can reattach to the airfoil surface, forming a laminar separation bubble (LSB) [3]. The transition process in an LSB is characterized by the convective amplification of disturbances through a Kelvin–Helmholtz instability in the separated shear layer [4,5]. This causes the shear layer to roll up into vortices, which experience three-dimensional deformations and undergo rapid turbulent breakdown in the aft portion of the LSB [6–8]. These vortices and their ensuing breakdown to turbulence enhance momentum exchange between the outer-flow and near-wall regions, and they can cause the separated shear layer to reattach to the airfoil surface in a mean sense, with a turbulent boundary layer forming downstream [1]. Between the mean locations of separation and turbulent reattachment is a region of recirculating flow associated with a plateau of relatively constant pressure [9].

The majority of studies has examined LSBs in two-dimensional geometric configurations [5,7,9–14]. However, finite-aspect-ratio effects are present in lifting surface applications such as aircraft wings and turbomachinery blades. Many recent studies on finite-aspect-ratio wings at low Reynolds number have focused on overall wing performance [15–20], finding that wing tip vortices suppress laminar separation near the wing tip [16,19] and contribute to nonlinearities in the lift curve [15]. The formation of a pressure plateau by the LSB is another source of nonlinear lift on finite-aspect-ratio wings [17]. Additionally, the lift-to-drag ratio, which is a critical performance parameter

Received 14 October 2020; revision received 31 December 2020; accepted for publication 5 January 2021; published online 19 April 2021.

*Graduate Student, Mechanical and Mechatronics Engineering, 200 University Avenue W.

†Graduate Student, Mechanical and Mechatronics Engineering, 200 University Avenue W. Student Member AIAA.

‡Professor, Mechanical and Mechatronics Engineering, 200 University Avenue W. Associate Fellow AIAA.

for lifting surfaces, is substantially reduced by laminar separation [2,21,22]. The importance of the LSB to the overall wing performance has been established in Refs. [15–20], but the effect of spanwise pressure gradients on the mean topology of an LSB and its dynamics have received little attention. Across the aforementioned studies, experimental findings on spanwise variations in separated shear layer characteristics and the associated vortex shedding process are limited, despite an expected significant influence from wing tip effects. For example, Awasthi et al. [23] considered a semispan wing with a very low aspect ratio of $AR = 0.5$ and concluded that the wing tip flow suppresses laminar separation, causing the formation of a region of high spanwise shear between the LSB and wing tip vortex. Marchman and Abtahi [24] were among the first to examine the aerodynamics of finite-aspect-ratio wings operating at low Reynolds numbers. Using surface oil flow visualization on a wing of $AR = 8$, they found two-dimensional flow with a high degree of spanwise uniformity approximately one chord length from the wing tip. Spanwise flow was confined to the region near the wing tips, which was similar to patterns seen at higher Reynolds numbers.

The spanwise pressure gradient and the associated downwash cause the reduction of sectional lift along the entire span of a finite wing compared to an equivalent airfoil section, with the largest decrease in lift occurring near the wing tip [25,26]. This effect is often quantified through the effective angle of attack, defined as the angle between the wing chord and the incident flow at a given spanwise location [26]. Previous investigations have shown that LSBs on two-dimensional airfoils are greatly influenced by the angle of attack since the airfoil's incidence to the flow largely governs the global streamwise pressure gradient on the suction surface [3]. At small angles of attack, the adverse pressure gradient on the suction surface is moderate, and laminar separation is delayed compared to higher angles of attack. As the angle of attack is increased, the adverse pressure gradient increases, and the LSB moves upstream and shortens [11]. The shortening of the bubble at higher angles of attack has been linked to decreased stability of the separated shear layer [5], which is related to the increase in boundary-layer edge velocity. This causes the mean locations of transition and reattachment to move upstream [27]. Furthermore, the central instability frequency of the separated shear layer, which defines the vortex rollup frequency, has been found to increase with the angle of attack [7,27]. Since the location and stability characteristics of LSBs on two-dimensional airfoils depend on the angle of attack, the changes in the effective angle of attack over the span of a finite wing are also expected to be critical in determining LSB behavior.

Bastedo and Mueller [28] conducted detailed surface pressure measurements at multiple spanwise locations on a semispan wing of $AR = 2$ and $0.14c$ thickness. They found that three-dimensional flow was confined to the outer 20% of the span, whereas the pressure distribution on the remaining portion of the wing was analogous to the pressure distribution characteristic of an LSB forming on the same two-dimensional airfoil section at a reduced angle of attack. Through surface oil flow visualization, they observed an LSB mean topology that changed gradually in the spanwise direction, forming a curved shape, with the locations of separation and reattachment moving downstream near the wing tip in response to the reduction in effective angle of attack at the wing tip. A similar LSB mean topology was observed in the surface oil flow visualization of Demir et al. [29], conducted on a wing of $AR = 3$ and $0.12c$ thickness. Garmann and Visbal [30] conducted an implicit large-eddy simulation of a plunging wing of $AR = 6$ and $0.12c$ thickness, finding that the LSB exhibited a small downstream shift near the wing tip. Huang and Lin [31] examined flow over an $AR = 5$ and $0.12c$ thick semispan wing through surface oil flow visualizations, finding that turbulent reattachment moved downstream near the tip while an upstream shift in the location of laminar separation near the wing tip was noted. Outside of the near-tip region, they reported that the LSB formed at a nearly constant chordwise location on the wing rather than the spanwise curved shape reported in Refs. [28,29].

The contrasting conclusions of the previous studies on the influence of the effective angle of attack on the LSB shape and location suggest that LSBs on finite wings may be influenced by additional effects not seen in nominally two-dimensional flows. Since the frequencies and growth rates of amplified disturbances in the separated shear layer are affected by the angle of attack [27], the response of the LSB on a finite wing to the effective angle of attack also has important implications for the transition process. This study seeks to determine how the LSB on a finite-aspect-ratio wing is influenced by wing tip effects and to characterize the associated spanwise structure of the LSB. Specific attention is paid to the relevance of the effective angle of attack to LSB dynamics on a finite wing. To this end, an experimental investigation was undertaken, employing surface pressure measurements and planar particle image velocimetry (PIV). Measurements were performed on an LSB formed on a NACA 0018 semispan wing of $AR = 2.5$ at $\alpha = 6$ deg and $Re_c = 1.25 \times 10^5$.

II. Experimental Methods

All measurements were conducted in the University of Waterloo recirculating wind tunnel, the test section of which is 2.44 m long, with a square cross section with a side length of 0.61 m. The freestream velocity was set according to a calibration between the static pressure drop across the wind tunnel's 9:1 contraction and the freestream velocity in the empty test section. All measurements were taken at a chord Reynolds number of $Re_c = 1.25 \times 10^5$, which corresponds to a freestream velocity of approximately 9.5 m s^{-1}. The uncertainty in freestream velocity was estimated to be less than 3%, and the turbulence intensity measured in the empty test section with a hot-wire probe was less than 0.08%.

An aluminum wing model with a NACA 0018 cross section, a chord length of 0.2 m, and a squared off wing tip was used. The wing had an aspect ratio of $AR = 2.5$ and was cantilevered from one of the side walls of the test section, leaving a gap of $0.5c$ between the wing tip and the opposing wall. An aspect ratio of 2.5 was chosen since pressure measurements on wings of $1.25 \leq AR \leq 2.75$ showed that $AR = 2.5$ is the minimum aspect ratio that provides a region of nominally two-dimensional flow near the wing root. To enable direct comparison with flow behavior on a two-dimensional airfoil, a removable wing extension was inserted that filled the gap between the tip of the aluminum wing model and the opposite wall of the test section, producing a nominally two-dimensional airfoil geometry. The extension was made from a plastic block with a NACA 0018 profile that matched the profile of the aluminum wing model. The surfaces of both the wing and the extension were polished to achieve consistent surface characteristics.

A baseline geometric angle of attack of $\alpha = 6$ deg was chosen, producing an LSB amenable to particle image velocimetry in terms of the spatial resolution of the measurements with respect to the overall length and height of the LSB. The angle of attack was set using a digital protractor. Repeated surface pressure measurements indicated that the angle of attack could be reliably set within ± 0.2 deg.

Two coordinate systems are used for data presentation. Side-view velocity results are presented using a surface-attached coordinate system defined with the origin at the wing root leading edge, with the positive x direction along the wing surface toward the trailing edge, the positive y direction normal to the suction surface, and the positive Z direction toward the wing tip. Top-view velocity results are presented in a two-dimensional chord-based coordinate system that has the same origin point and Z axis as the surface-attached system but differs in that the X axis is parallel to the chord of the model. All coordinate axes are shown in Fig. 1.

A. Surface Pressure Measurements

Surface pressure measurements on the model were performed using 89 static pressure taps (0.4 mm in diameter), whose layout is shown in Fig. 1a. For chordwise pressure measurements, the 65 pressure taps arranged in a staggered configuration at $Z/c = 0.95$ on both the suction and pressure surfaces (dashed line in Fig. 1a) were used. The remaining pressure taps were divided among three spanwise rows on the suction surface at $X/c = 0.15$, 0.30, and 0.60 (markers in Fig. 1a); and they were used to measure the suction-side spanwise pressure distribution. The pressure taps were connected to two Setra model 239 pressure transducers with input ranges of

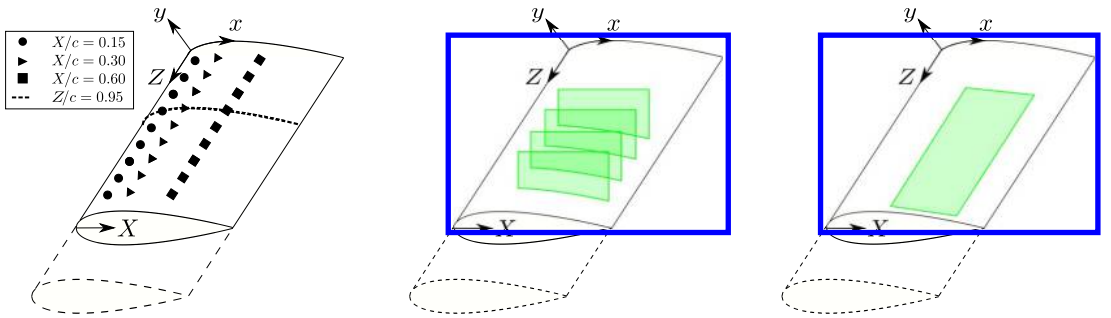

a) Locations of pressure taps b) Side-view PIV c) Top-view PIV

Fig. 1 Experimental model configurations. Thin dashed line shows the wing extension used for the two-dimensional airfoil configuration.

± 250 Pa via two Scanivalve multiplexers. Pressure transducer outputs were measured using a National Instruments USB-6259 data acquisition system. For all pressure measurements, a total of 4000 samples were acquired at each tap location at a sampling frequency of 1 kHz. The uncertainty in the obtained surface pressure distributions was estimated to be less than 1.4% of the freestream dynamic pressure.

B. Particle Image Velocimetry Measurements

Two-component planar PIV measurements were performed in two different configurations (Figs. 1b and 1c), referred to as the side and top views. For the side-view configuration, the light sheet was positioned in $x - y$ planes at $Z/c = 0.95$, 1.30, 1.66, and 2.01 (Fig. 1b), with the spanwise locations chosen to cover an area of the wing outside of the direct influence of root and tip flows, as well as to avoid laser light reflections from the pressure taps on the airfoil surface. At $Z/c = 0.95$, the light sheet was positioned between the staggered chordwise pressure taps. In the side-view configuration, measurements were performed at the baseline angle of attack ($\alpha = 6.0$ deg) at all spanwise locations for both the wing and airfoil model configurations. Furthermore, additional measurements at $Z/c = 0.95$ were performed over a range of angles of attack (3.8 deg $\leq \alpha \leq$ 5.0 deg) on the two-dimensional airfoil configuration covering the expected effective angle-of-attack range at the PIV measurement locations on the finite wing model configuration.

Top-view PIV measurements were conducted with the light sheet positioned tangent to the suction surface of the wing, as shown in Fig. 1c. The minimum distance between the light sheet and the surface of the wing model was $0.007c$. This positioning was selected such that the measurement plane passed through the top halves of the shear layer rollup vortices observed in the side-view measurements. Top-view PIV measurements were conducted on both the finite wing and the two-dimensional airfoil configurations at $\alpha = 6.0$ deg.

For all PIV measurements, the flow was seeded with water–glycol-based fog, and particle illumination was provided by a Photonics DM20-527 neodymium-doped yttrium lithium fluoride (Nd:YLF) pulsed laser. The laser light was formed into a sheet approximately 1.5 and 2 mm thick for the side-view and top-view configurations, respectively. Synchronization of the cameras and laser was provided by a LaVision timing unit. Table 1 provides an overview of the PIV parameters used in both configurations.

In the side-view configuration, two 1.0 megapixel Photron FastCam SA4 high-speed cameras were used with 200 mm macrolenses. The camera sensors were cropped to 1024×512 pixels. The cameras' fields of view were overlapped by $0.016c$ (9%), resulting in a total field of view that spanned $0.23 \leq x/c \leq 0.58$, and from the model surface to $y/c = 0.08$. A total of 5457 samples were taken at both 3.88 and 0.3 kHz for spectral analysis and statistics, respectively. Based on the nominal shedding period within the LSB of 2 μs, over 1000 shedding cycles are captured within the time-resolved PIV measurements, whereas measurements at the lower sampling rate provide statistically independent samples for statistics.

To capture a larger field of view in the top-view PIV configuration, two 5.5 megapixel LaVision Imager scientific complimentary metal-oxide semiconductor (sCMOS) cameras were used, which were equipped with 50 mm macrolenses. The camera sensors were cropped to 2560×1492 pixels. With an overlap of approximately $0.059c$ (7%), the total field of view for top-view PIV measurements spanned $0.28 \leq X/c \leq 0.71$ and from $0.93 \leq Z/c \leq 2.5$. Sampling was performed at 36 Hz, with a total of 4888 samples collected per measurement set.

LaVision's DaVis software was used for image acquisition and processing. Side-view particle images were preprocessed using a sliding minimum subtraction, whereas the top-view particle images were preprocessed using a high-pass filter with a cutoff frequency of 5 Hz. Velocity fields were then calculated from the images using multipass cross correlation with window deformation [32]. The final interrogation window sizes were 16×16 pixels and 32×32 pixels for the side-view and top-view configurations, respectively, with 75% window overlap. The velocity fields were postprocessed using iterative outlier detection and removal based on the median filter method [33]. The resulting vector fields were then stitched together using cosine blending in the overlap region. For data analysis and presentation, the side-view velocity fields were transformed into the surface attached coordinate system (Fig. 1b). All velocity spectra were computed from the PIV measurements using Welch's method [34] with 20 windows of 512 samples with 50% overlap. With 50% overlap, the variance of the Welch's power spectral density estimate approximately follows a χ^2 distribution with the number of degrees of freedom equal to twice the number of windows [35]. The corresponding uncertainty in spectral magnitude is estimated to be between 67 and 164%, and the frequency resolution of the velocity spectra is ± 3.8 Hz.

Using the correlation statistics method [36], the random errors in the PIV measurements were estimated to be less than 4 and 9% of the freestream velocity for the side- and top-view configurations, respectively. Uncertainties of quantities derived from the PIV measurements were calculated using sequential perturbation [37]. The dominant uncertainty in the integral boundary-layer parameters and mean locations of separation and reattachment stems from location of the model

Table 1 PIV measurement parameters

Parameter	Side view	Top view
Camera	(Two) Photron FastCam SA4	(Two) LaVision imager sCMOS
Sensor resolution, pixels	1024×512	2560×1492
PIV mode	Double frame	
Frame separation, μs	60	45
Sampling rate, Hz	3880 and 300	36
Sampling time, s	1.41 and 18.19	124.77
Lens focal length, mm	200	50
Magnification factor	0.51	0.10
Combined field of view	$0.35c \times 0.08c$	$1.57c \times 0.43c$
Laser	Photonics DM20-527 Nd:YLF	
Light sheet thickness	≈1.5 mm	≈2 mm
Seeding particles	Water–glycol fog	
Final interrogation window size, pixels	16×16	32×32
Window overlap, %	75	75
Vector pitch, mm	0.16	0.51

surface in the PIV images, which could be located to within ±0.2 mm (±0.001c) in the y direction and ±1 mm (±0.005c) in the X direction.

III. Results

Surface pressure and planar PIV measurements are presented for a semispan NACA 0018 wing with an aspect ratio of $AR = 2.5$ at a geometric angle of attack of $\alpha = 6$ deg and a chord Reynolds number of $Re_c = 1.25 \times 10^5$. Measurements are also performed using a two-dimensional model configuration over a range of angles of attack encompassing the effective angles on the wing, allowing for an examination of finite wing effects on LSB mean topology and dynamics. Throughout the presentation of results, the two-dimensional airfoil and $AR = 2.5$ wing configurations are referred to as the airfoil and wing, respectively.

A. Surface Pressure Distributions

Figure 2a contrasts the chordwise surface pressure distributions on the wing and the airfoil at the same geometric angle of attack. For both cases, the pressure distribution on the suction side features a characteristic pressure plateau downstream of the suction peak, indicating the presence of an LSB [9]. Measurements on the pressure surface indicate that there is no LSB present on the pressure side of the airfoil. As expected, Fig. 2a indicates that the suction peak magnitude is reduced on the finite wing [17,28], and the accompanying changes in the pressure gradient result in the notable downstream shift of the pressure plateau. This indicates the downstream shift of the LSB, consistent with the expected decrease of the effective angle of attack [28].

Figure 2b shows the spanwise pressure distributions on the suction surface from the three spanwise rows of pressure taps. The locations of the streamwise pressure taps are indicated by the dashed line in Fig. 2b, whereas pressures common to the measured streamwise and spanwise distributions are marked in Fig. 2a. From Fig. 2a, the rows at $X/c = 0.15$ and 0.60 are located upstream and downstream of the expected LSB location, respectively, whereas the middle row ($X/c = 0.3$) is located within the LSB. The airfoil configuration displays spanwise uniform pressure distributions at $X/c = 0.15$ and 0.60; however, an increase in suction on the airfoil within the LSB at $Z/c = 2.25$ and $X/c = 0.30$ is observed. This increase is attributed to the high degree of sensitivity of LSBs to test environment perturbations [11] since the surface pressures outside of the LSB remain virtually constant across the span of the airfoil. For the wing configuration, suction-side pressure magnitudes are decreased compared to those of the airfoil configuration, whereas a gradual decrease in suction is observed with increasing Z/c (i.e., toward the wing tip), which is consistent with the expected spanwise pressure gradient on finite wings [25,28].

The results in Fig. 2a indicate that the sectional lift coefficients of the wing are lower than those of the airfoil, with the difference expected to increase as the wing tip is approached. This decrease in sectional lift is commonly represented as a decrease in the effective angle of attack [26]. Therefore, if an estimate of the spanwise variation in the effective angle of attack is available for the wing, then conditions under which the airfoil and wing models produce similar streamwise pressure distributions can be identified. At these conditions, LSB characteristics can be cross examined between the airfoil and wing, allowing for the effect of the spanwise pressure gradient to be isolated.

B. Estimation of Effective Angle of Attack

The variation in the effective angle of attack along the span of the wing model at a geometric angle of attack of $\alpha = 6$ deg is determined using the following procedure. First, a set of baseline pressure distributions is established for the airfoil over a range of geometric angles of attack. Then, for each spanwise location on the wing at which spanwise pressure taps are situated ($Z/c = 0.25$, 0.50, 0.75, etc.), the three data points available in the streamwise direction are compared with the airfoil data to identify the closest match. When the data are matched, the geometric angle of attack of the corresponding airfoil pressure data is taken as the effective angle of attack at the examined Z/c location on the wing.

From an initial exploratory survey, the effective angle of attack on the wing in the region of $0.95 \leq Z/c \leq 2.01$ was estimated to fall in the range 4 deg $\leq \alpha_{\text{eff}} \leq 5$ deg. Thus, a refined sweep of pressure measurements on the airfoil was performed around this angle-of-attack range, and the obtained data were used for a detailed matching procedure. First, the pressure data from the three pressure taps on the airfoil common to the streamwise and spanwise rows are considered, with Fig. 3 showing the pressure coefficients from these three locations plotted against α. Also plotted in Fig. 3 (inset plots) are streamwise pressure distributions for a select number of angles of attack. Given the nearly linear variation of the pressure coefficients within this range of angles of attack (blue lines in Fig. 3), the effective angle of attack on the wing is estimated at all Z/c locations at which pressure data are available by finding the value of α that minimized the sum of squared differences between the linear fits (determined from the airfoil pressure measurements) to the wing pressure measurements at a specific Z/c location. This is illustrated in Fig. 4a, where the three pressure measurements at a single spanwise location on the wing (red markers) are shifted horizontally such that the sum of squares of Δ_1, Δ_2, and Δ_3 is minimized, thus identifying the effective angle of attack for this spanwise location. Figure 4b shows the results for all spanwise pressure tap locations on the wing. It should be noted that the wing pressure coefficients at the same three streamwise locations also exhibit a nearly linear variation with the effective angle of attack, supporting the employed approach.

Figure 5 presents the obtained variation of the effective angle of attack along the span of the wing, with the indicated uncertainly limits incorporating estimates of both the measurement and methodological uncertainty. The locations of the PIV measurement planes are indicated by the vertical dotted lines. Since the lifting line theory has been shown to produce reasonable estimates of the effective angle of attack

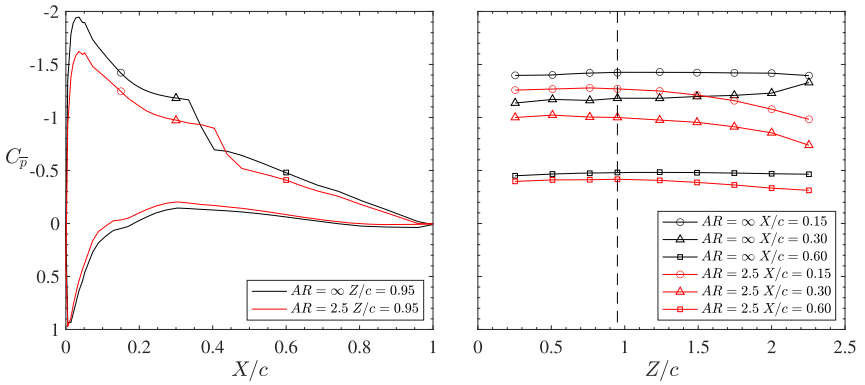

a) Streamwise distribution **b) Spanwise distribution**

Fig. 2 Surface pressure distributions at $\alpha = 6$ deg on wing and airfoil. Symbols in Fig. 2a mark measurements common to streamwise and spanwise distributions. Dashed line in Fig. 2b shows spanwise location of measurements presented in Fig. 2a.

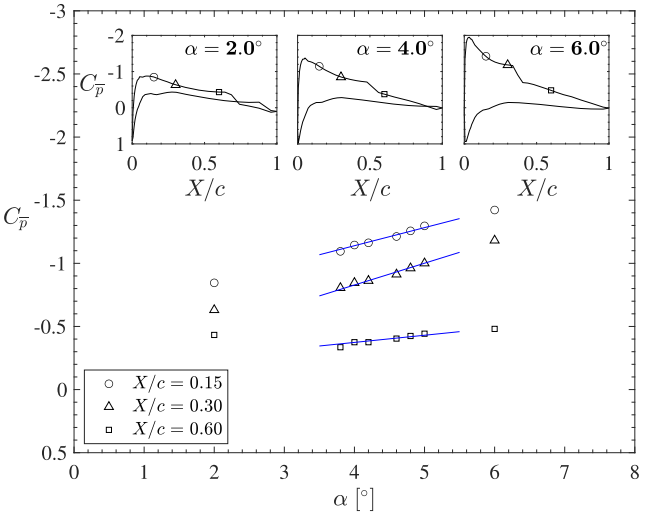

Fig. 3 Surface pressure coefficient versus angle of attack for the airfoil. Linear fits (in blue) are applied to the data in the range $3.8 \leq \alpha \leq 5$. Inset plots show representative streamwise pressure distributions.

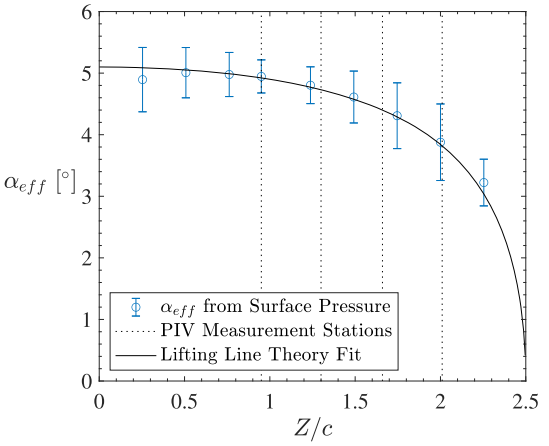

Fig. 5 Spanwise variation of effective angle of attack on the wing. Dashed lines indicate spanwise locations of PIV measurements. Solid line is a least-squares fit from lifting line theory for rectangular wings.

on the outboard region of finite wings with LSBs [23], it is employed in the present investigation to support α_{eff} estimates. In applying the lifting line theory, the effective angle of attack along the span of an untwisted wing with a symmetric airfoil profile can be predicted by solving the following system of equations [26,38]:

$$\sum_{n=1}^{N} A_n \sin(n\phi_i)(\mu_i n + \sin(\phi_i)) = \alpha\mu_i \sin(\phi_i), \qquad i = 1, 2, \ldots, N \tag{1}$$

where i denotes each of the N control points in the spanwise direction, $\phi_i = \arccos(Z_i/s)$ with s being the wing semispan, and $\mu_i = c(\partial C_l/\partial\alpha)/(8s)$. The sectional lift coefficient C_l corresponds to a two-dimensional airfoil, where the angle of attack α is the geometric angle of attack. The exact lifting line solution is obtained as $N \to \infty$. By solving Eq. (1) for the coefficients A_n, which are related to the circulation, the effective angle of attack at each spanwise control point i can be obtained using the following relationship [38]:

$$\alpha_{\text{eff},i} = \sum_{n=1}^{N} nA_n \frac{\sin(n\phi_i)}{\sin(\phi_i)} \tag{2}$$

In this process, it is important to account for tunnel wall interference effects [39]. Here, because of the linear relation between α and $\alpha_{\text{eff},i}$ and the consequent similarity of the solution for a given α, an iterative approach was used, where the value of α was iteratively changed in Eq. (1) to obtain the best fit between the solution of Eq. (2)

Table 2 Estimated α_{eff} at each side-view PIV measurement station

Z/c	α_{eff}, deg
0.95	4.9
1.30	4.7
1.66	4.4
2.01	3.8

and estimates of the effective angle in Fig. 5. The value of α obtained was 6.6 deg, with the difference from the true geometric angle of attack ($\alpha = 6.0$ deg) verified to be in close agreement with the estimated effective angle-of-attack change due to wall interference [39]. A comparison of the results in Fig. 5 shows that the lifting line theory fit conforms well to the pressure-based estimates, which lends further support to the applicability of the lifting line theory to wings operating at low Reynolds numbers and provides added confidence in the obtained distribution of the effective angles of attack. The estimates of α_{eff} at the locations of the side-view PIV measurements taken from the lifting line theory curve fit in Fig. 5 are summarized in Table 2, and they are used to compare measurements on the airfoil and wing in Secs. III.C and III.D.

C. Mean Velocity Field

Mean streamwise velocity contours in the area of LSB formation are presented for the airfoil and wing in Figs. 6a and 6b, respectively, for a comparable range of effective angles of attack. The LSB is identified by the mean dividing streamline (solid black line), defined as the locus of points below which there is zero net mass flow across

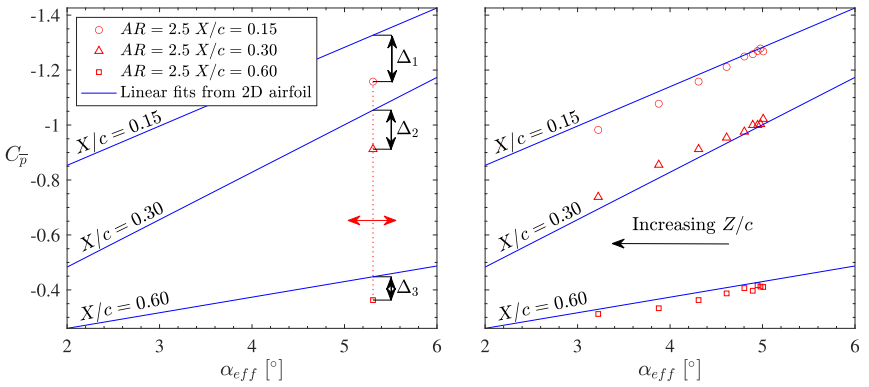

a) Methodology **b) All spanwise pressure tap locations**

Fig. 4 Estimation of effective angle of attack on the wing.

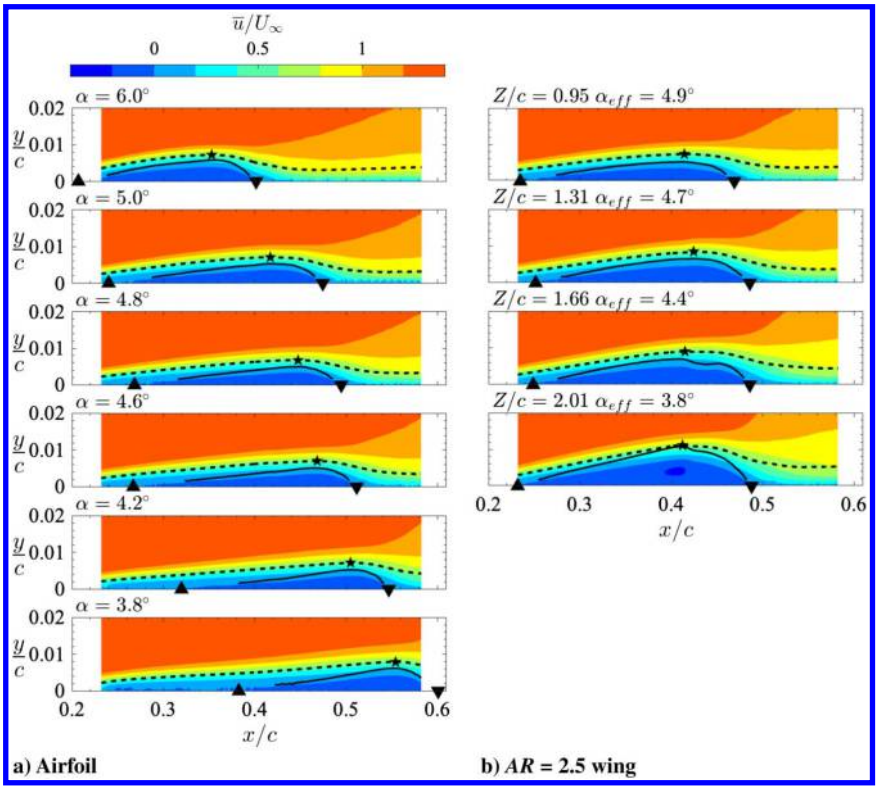

Fig. 6 Contours of mean streamwise velocity. Solid lines indicate mean dividing streamline and dashed lines indicate displacement thickness: $\overline{x_t}$ (stars), $\overline{x_s}$ (upward-pointing triangle), and $\overline{x_r}$ (downward-pointing triangle).

any wall-normal plane [9]. Separation and reattachment locations were estimated by extrapolating the dividing streamline to the model surface via a smoothing spline fit. The transition location was estimated from the location of maximum displacement thickness, which has been shown to correspond to the location of pressure recovery onset [5] and vortex rollup [40]. As expected from the pressure distributions (inset plots in Fig. 3), as well as trends reported in previous studies on various airfoils [11,27,41], the LSB moves downstream and lengthens as the angle of attack is decreased on the airfoil model configuration (Fig. 6a). In contrast, at the four surveyed spanwise planes on the wing model (Fig. 6b), the LSB remains at approximately the same streamwise location across the span, whereas an increase in the maximum displacement thickness and mean reverse flow velocity is observed with increasing Z/c and decreasing α_{eff}.

For comparison, the mean locations of separation, transition, and reattachment are presented in Fig. 7, where they are plotted against the angle of attack and effective angle of attack for the airfoil and wing, respectively. The results confirm and quantify the downstream movement of the LSB with decreasing angle of attack on the airfoil. For the wing model, over a change in effective angle of attack of 1.1 deg, minimal changes in the LSB characteristics are observed, which are in stark contrast to the trends seen in the LSB characteristics on the two-dimensional model when the angle of attack is changed by a similar amount. In fact, the spanwise variations of the mean separation, transition, and reattachment locations on the wing were verified to be comparable to the spanwise variations on the airfoil at $\alpha = 6.0$ deg. However, the results point to distinct similarities between the LSBs formed at equal values of α and α_{eff} for the airfoil and wing in the region away from the wing tip. In particular, at $\alpha_{\text{eff}} = 4.9$ deg, the measurements performed on the wing at $Z/c = 0.95$ yield similar results to those obtained on the airfoil model at $\alpha = 5$ deg (Fig. 7) because the mean streamwise velocity contours (Fig. 6) are remarkably similar between these cases, leading to closely matching mean LSB characteristics (Fig. 7). Thus, the results suggest that a quantitative similarity in mean LSB topology between the airfoil and wing is restricted to the region of weakly three-dimensional flow away from the wing tip. As the spanwise gradient in the effective angle becomes progressively more significant near the wing tip, such

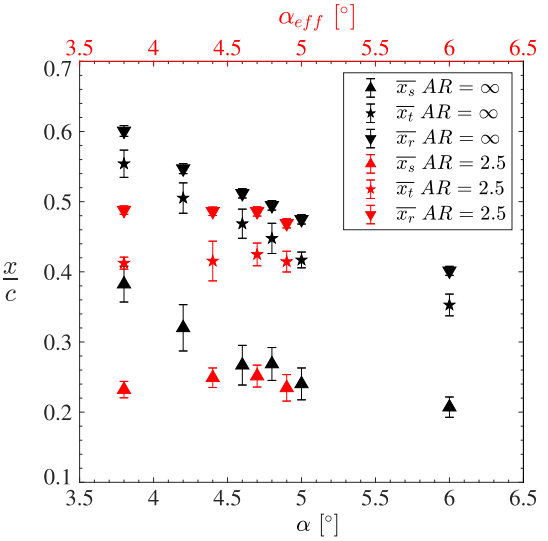

Fig. 7 Locations of mean separation, transition, and reattachment on the airfoil at 3.8 deg $\leq \alpha \leq$ 6 deg and wing at $\alpha = 6$ deg. Markers colored according to the x axis on which they are plotted.

a similarity breaks down. This important finding provides quantitative support to the results reported in Refs. [17,24,31], and it suggests that the analogy between LSBs at the same effective angle of attack suggested in Ref. [28] is not universal. In fact, over the spanwise range considered in this study, the effective angle of attack of the wing root can be used to accurately describe the mean locations of separation, transition, and reattachment up to at least $Z/c = 2.01$, despite the substantial reduction in α_{eff}.

In comparison to the airfoil configuration at the same effective angle of attack, the differences in LSB position on the wing are most significant near the tip (low effective angles of attack in Fig. 7). Here, three-dimensional effects and the spanwise pressure gradient are most significant on the wing; however, the exact mechanism responsible for

the associated changes in LSB location merits future investigation. It should be noted that in the present analysis, the locations of separation and reattachment are based on classical estimations of the locations of zero in-plane wall shear, which can differ in strongly three-dimensional flows [42]. Future measurements of the spanwise velocity component in the LSB should be conducted to provide further insight into how the spanwise pressure gradient affects LSB structure, and to determine whether the calculated locations of separation and reattachment are biased by spanwise flow within the LSB.

The variation in displacement thickness on the airfoil with the angle of attack is presented in Fig. 8a. The maximum displacement thickness does not show any significant changes within the investigated range of airfoil incidences. On the other hand, a clear trend of increasing maximum displacement thickness with increasing Z/c is observed within the range of $0.95 \leq Z/c \leq 2.01$ on the wing in Fig. 8b. The associated displacement of the separated shear layer away from the airfoil surface is also accompanied by an increase in maximum mean reverse flow magnitude, as seen in Fig. 6b, particularly at $Z/c = 2.01$. Such changes are known to affect stability characteristics of near-wall shear flows [13,43,44] and even the nature of the dominant flow instability mode [12,45]. At the same time, the characteristic mean locations of the bubble appear to remain invariant within experimental uncertainty, which points to a likely interplay between wing tip effects and changes in stability in this region. The potential implication these changes have on bubble dynamics will be explored in Sec. III.D.

The observed changes in maximum displacement thickness and reverse flow velocity near the tip of the wing suggest that three-dimensional effects are important to LSB development in the vicinity of the wing tip, where a considerable spanwise pressure gradient is observed (Fig. 2b). Using the top-view PIV configuration (Fig. 1c), measurements of streamwise and spanwise flows were made above a portion of the airfoil and wing surfaces at $\alpha = 6.0$ deg, with time-averaged flowfields presented in Fig. 9. This figure shows sectional streamlines superimposed onto contours of mean spanwise flow velocity. The results verify two-dimensional flow for the airfoil, and they confirm the presence of a crossflow that progressively increases in magnitude near the wing tip. The isolation of significant spanwise flow to $2.2 \leq Z/c \leq 2.5$ agrees with the findings of Bastedo and Mueller [28], who observed that the three-dimensional flow region is limited to a distance of less than $0.4c$ from the wing tip at moderate angles of attack. At the outermost side-view PIV measurement station ($Z/c = 2.01$), the mean spanwise velocity magnitude on the wing remains below 7% of U_∞ (Fig. 9b); however, it produces substantial changes to the mean LSB outline seen in side-view measurements (Fig. 6b). Therefore, a relatively small magnitude of spanwise flow can lead to dissimilar LSBs on two-dimensional airfoils and finite-aspect-ratio wings at the same effective angle of attack, with progressively larger differences expected as the wing tip is approached.

D. Separation Bubble Dynamics

The vortex shedding in the LSB is examined in Figs. 10 and 11, where sequences of instantaneous spanwise vorticity are presented for the airfoil and wing configurations, respectively. On the airfoil (Fig. 10), the formation and shedding of shear layer vortices can be clearly seen in Fig. 10a, corresponding to $\alpha = 5.0$ deg. The shear layer rolls up at approximately the location of maximum mean bubble height ($x/c = 0.40$) and the shed vortices propagate downstream, marked by dashed lines connecting the same structures in the sequence. A similar dynamics is captured on the wing at a similar effective angle of attack (Fig. 11a), with a comparable rollup location and streamwise wavelength of the structures observed for this spanwise location, which is subject to a minimal spanwise flow (Fig. 9). As expected from the time-averaged results discussed earlier, decreasing the angle of attack of the airfoil results in the downstream movement of the rollup location, which can be seed from a comparison of Figs. 10a and 10b. In contrast, for the wing configuration, the rollup location remains largely insensitive to the decrease in the effective angle of attack (Fig. 11). However, the increase in maximum displacement thickness at $Z/c = 2.01$ is associated with the formation of rollup vortices farther from the wing surface compared to that at $Z/c = 0.95$.

The rms fluctuating velocity fields for the airfoil and wing are shown in Figs. 12 and 13. Both cases show a significant increase in the amplitude of the fluctuations in the aft portion of the separation bubble. The rapid growth in the magnitudes of u'_{RMS} and v'_{RMS} is most prominent near the location of mean transition, which is coincidental with the shear layer rollup seen in Figs. 10 and 11. At a fixed x/c location in the vicinity of $\overline{x_t}$, three peaks are seen in the u'_{RMS} fields for both airfoil and wing configurations, which is in agreement with previous experimental studies [8,46] and eigenmodes obtained in linear stability calculations [4,5]. The most significant fluctuations in

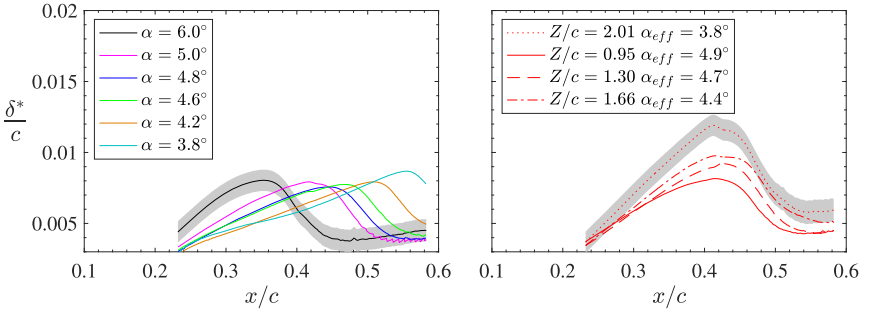

a) Airfoil **b) *AR* = 2.5 wing**

Fig. 8 Streamwise displacement thickness. Shaded areas show typical uncertainty bounds.

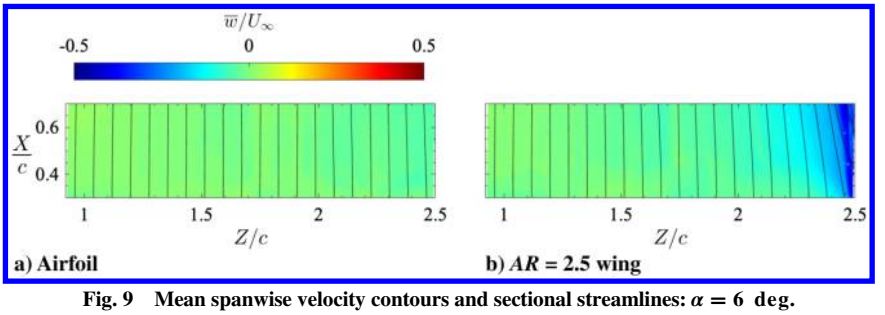

a) Airfoil **b) *AR* = 2.5 wing**

Fig. 9 Mean spanwise velocity contours and sectional streamlines: $\alpha = 6$ deg.

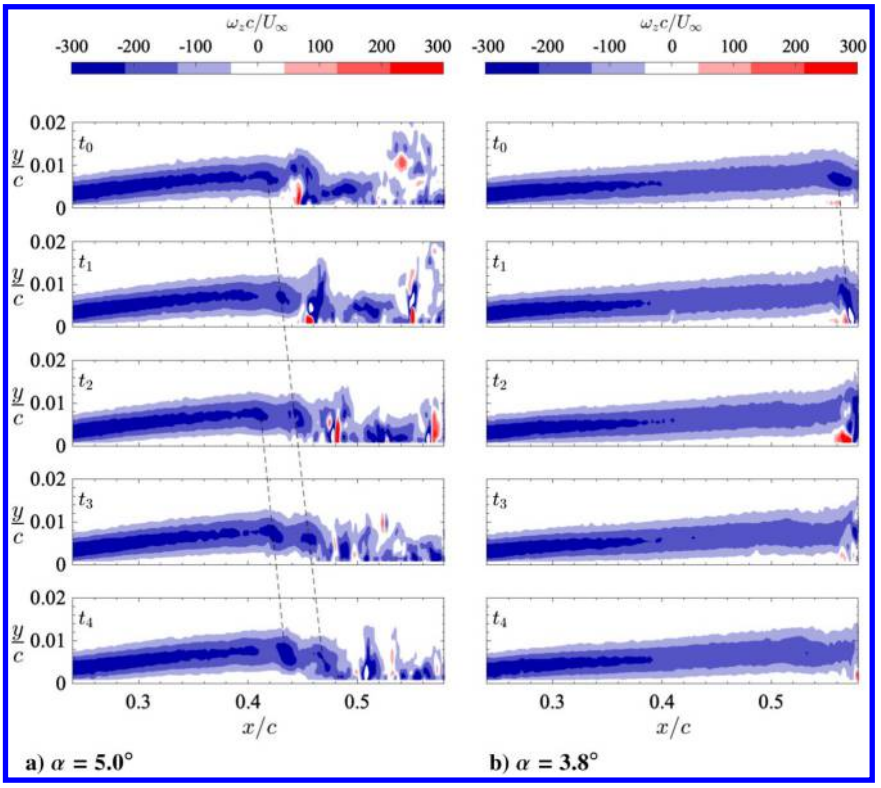

Fig. 10 Contours of instantaneous vorticity on the airfoil. Frame separation is 0.13 ms. Dashed lines track individual vortices.

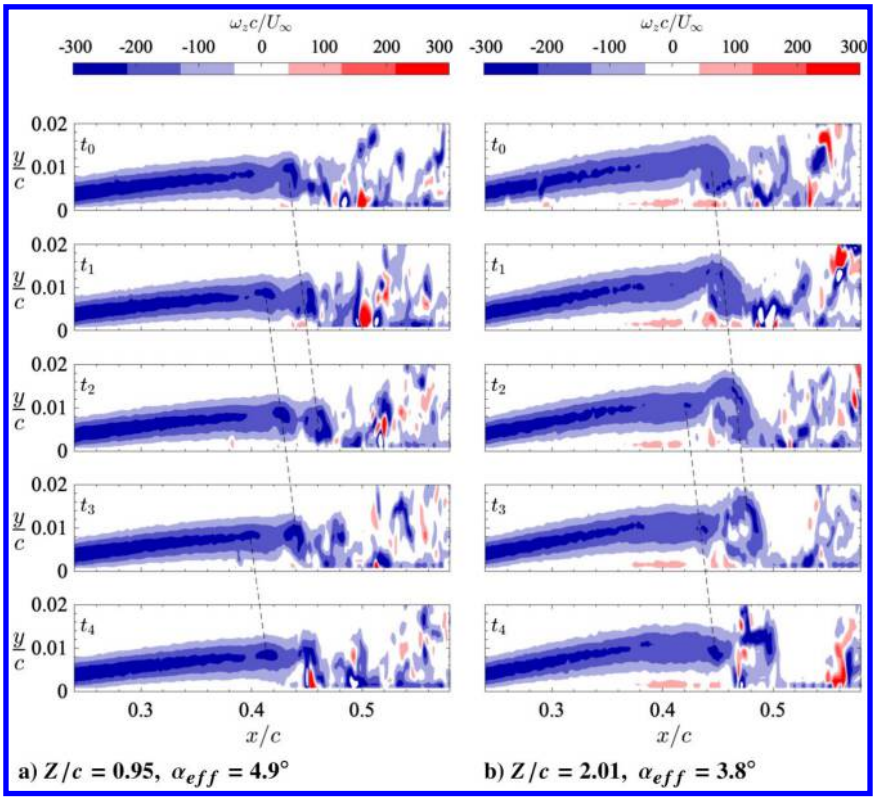

Fig. 11 Contours of instantaneous vorticity on the wing. Frame separation is 0.13 ms. Dashed lines track individual vortices.

the streamwise velocity component (Fig. 12) closely follow the boundary-layer displacement thickness (marked by the dashed line), outlining the trajectory of convectively amplified perturbations in the separated shear layer. For the wall-normal velocity fluctuations (Fig. 13), the maximum is reached at approximately the mean reattachment location, where vortices are shed into the redeveloping turbulent boundary layer. For the airfoil, the location of the onset of significant velocity fluctuations moves downstream with decreasing angle of attack, following the downstream movement of the mean transition and the mean reattachment locations. For the wing, consistent with the location of mean transition remaining relatively constant across the span, the rms velocity contours indicate that the

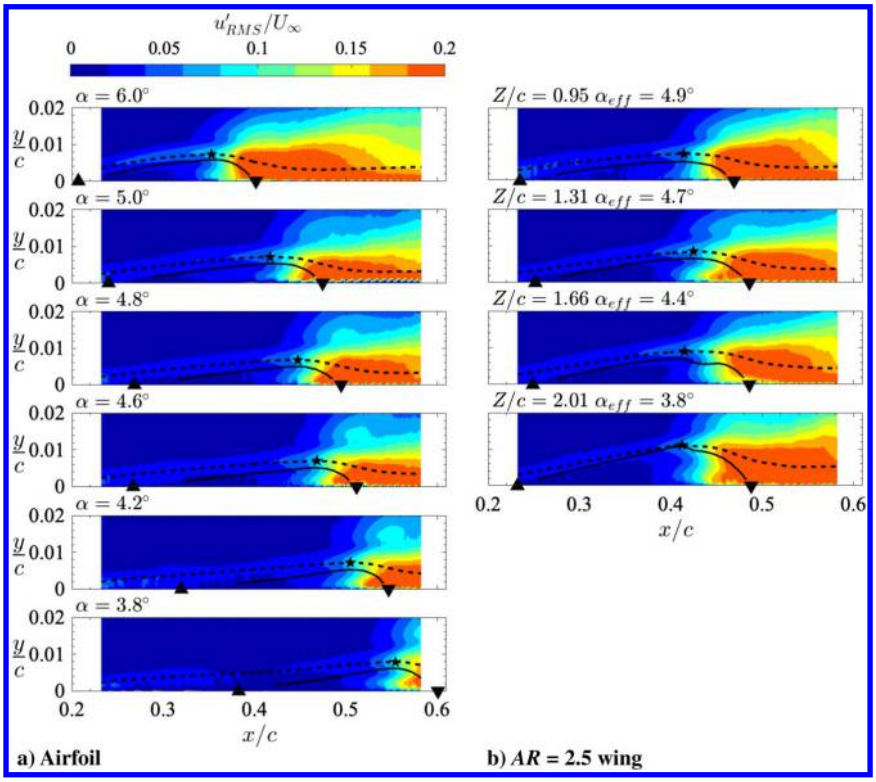

Fig. 12 Contours of rms streamwise velocity fluctuations. Solid lines indicate mean dividing streamline and dashed lines indicate displacement thickness: $\overline{x_t}$ (stars), $\overline{x_s}$ (upward-pointing triangle), and $\overline{x_r}$ (downward-pointing triangle).

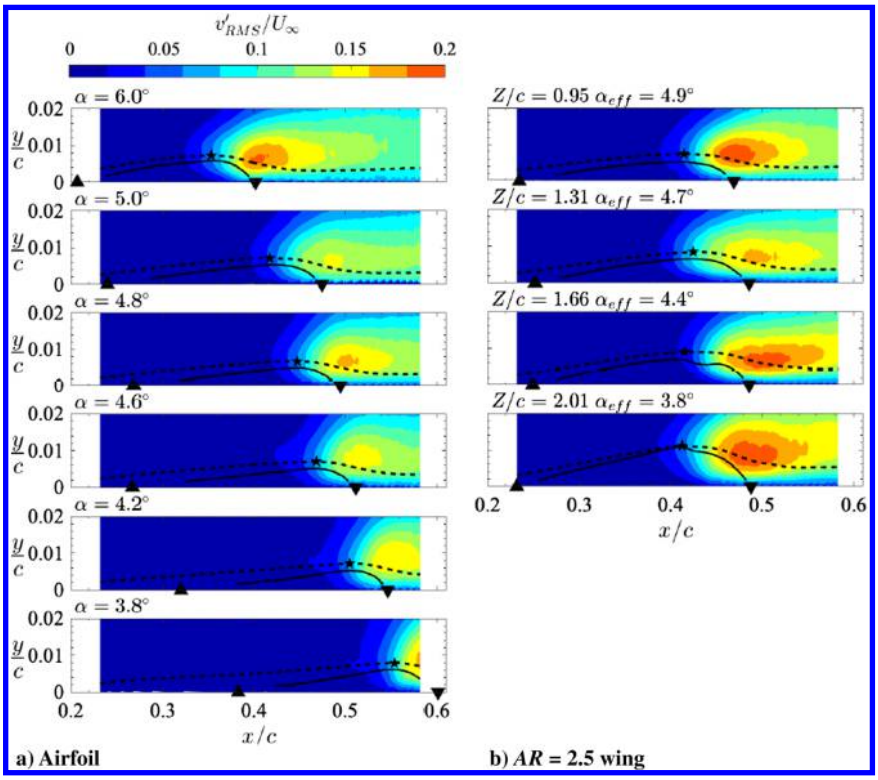

Fig. 13 Contours of rms wall-normal velocity fluctuations. Solid lines indicate mean dividing streamline and dashed lines indicate displacement thickness: $\overline{x_t}$ (stars), $\overline{x_s}$ (upward-pointing triangle), and $\overline{x_r}$ (downward-pointing triangle).

location of rapid growth of turbulent fluctuations remains largely unchanged as the effective angle of attack changes from 4.9 to 3.8 deg. Although the rms velocity contours on the wing closely resemble those obtained on the airfoil at $\alpha = 5.0$ deg, the vertical extent of the region associated with the highest contours of u'_{RMS} and v'_{RMS} is larger on the wing, and it increases toward the wing tip. This correlates with the increase in the displacement thickness (Fig. 8b), which is expected to result in a more unstable shear layer (i.e., higher amplifications factors [13,44]).

Spectral analysis of velocity fluctuations measured in the separated shear layer is performed to explore potential differences in the frequency content and amplitude of the amplified disturbances

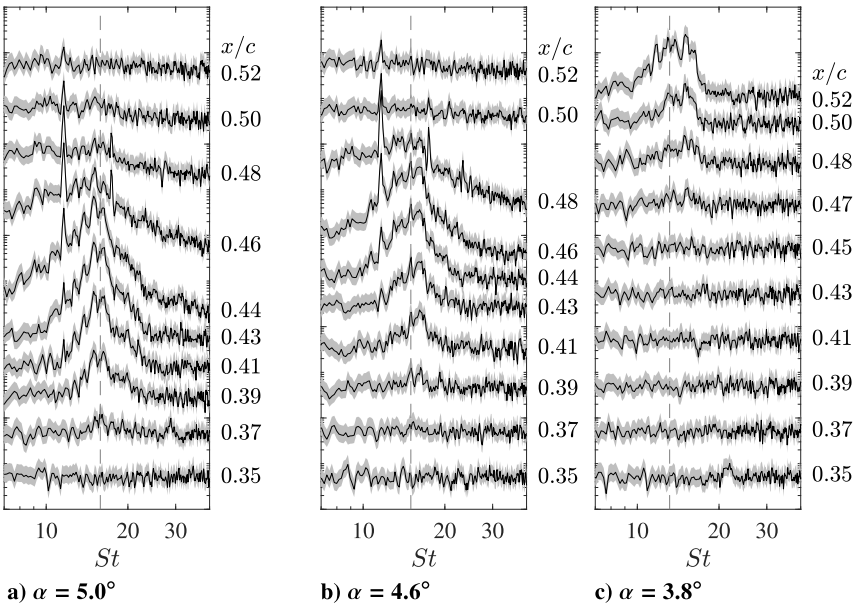

Fig. 14 Spectra of surface-normal velocity fluctuations at $y = \delta^*$ on airfoil: each spectrum normalized by its total energy content and each x/c location stepped by an order of magnitude for clarity. Dashed lines indicate St_0. Shaded regions indicate uncertainty in power spectral density magnitude.

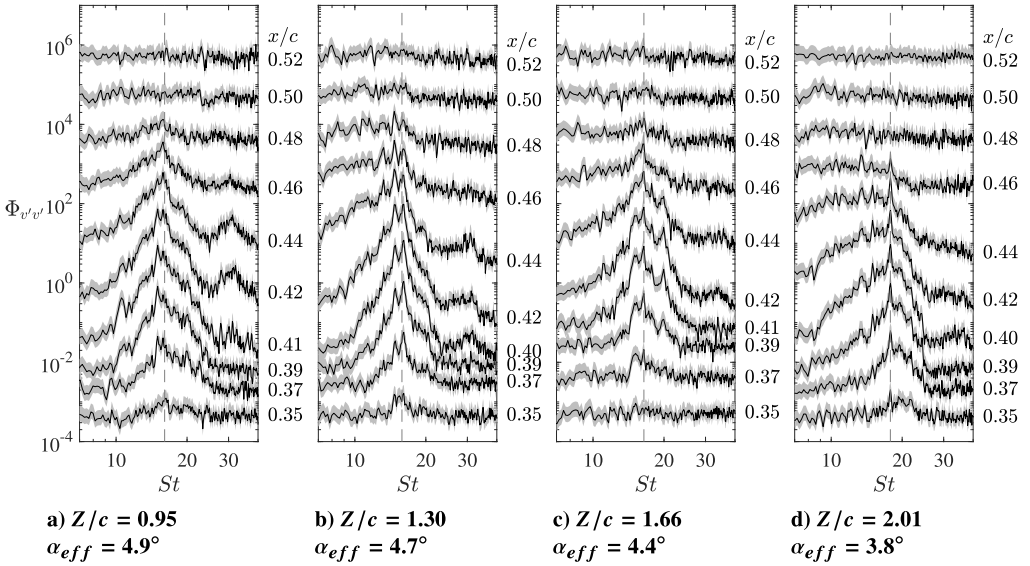

Fig. 15 Spectra of surface-normal velocity fluctuations at $y = \delta^*$ on wing at $\alpha = 6$ deg: each spectrum normalized by its total energy content and each x/c location stepped by an order of magnitude for clarity. Dashed lines indicate St_0. Shaded regions indicate uncertainty in power spectral density magnitude.

between the airfoil and wing configurations. Figure 14 presents spectra of wall-normal velocity fluctuations at $y = \delta^*$ for the airfoil at three angles of attack, with frequency presented in terms of the Strouhal number. The results show the amplification of disturbances within a band of frequencies, with the central instability frequency of the band marked by a dashed line. As the angle of attack of the airfoil decreases from $\alpha = 5.0$ deg to $\alpha = 3.8$ deg, the onset of disturbance amplification occurs farther downstream (c.f. spectra at $x/c = 0.41$ for Figs. 14a–14c), and the central instability frequency decreases from $St_0 = 15.9$ to $St_0 = 13.4$, in agreement with the trends reported in previous studies [7,27]. In contrast, the spectra of wall-normal velocity fluctuations in the separated shear layer of the wing (Fig. 15) do not show a marked change in the central instability frequency with decreasing effective angle of attack, nor the accompanying delay in the amplification of the perturbations.

Figure 16 shows the central instability frequency plotted for the airfoil and wing as a function of angle of attack and effective angle of attack, respectively. The results for the airfoil show a nearly linear increase in St_0 with increasing angle of attack, closely following the trends seen in the results taken from previous studies of the same airfoil over a similar range of Reynolds numbers. For the wing at $Z/c = 0.95$, where $\alpha_{\text{eff}} = 4.9$ deg, the central instability frequency closely matches the central instability frequency of the airfoil at $\alpha = 5.0$. As the effective angle of attack decreases toward the wing tip, the central instability frequency on the wing remains within the range $16.1 \leq St_0 \leq 17.8$ over the spanwise extent of side-view PIV measurements. This variation of the central instability frequency along the span of the wing is largely captured by the experimental uncertainty and was verified to be comparable to the spanwise variation on the airfoil at the same geometric angle of attack.

Figure 17 facilitates a more detailed comparison of wall-normal velocity fluctuation spectra obtained at the same streamwise positions in the separated shear layer at different spanwise locations on the wing at $\alpha = 6$ deg and on the airfoil at $\alpha = 5.0$ deg. All spectra presented in Fig. 17 were taken at $\overline{x_t}$ and $y = \delta^*$. The bands of amplified frequencies at spanwise locations of $Z/c \leq 1.30$ from

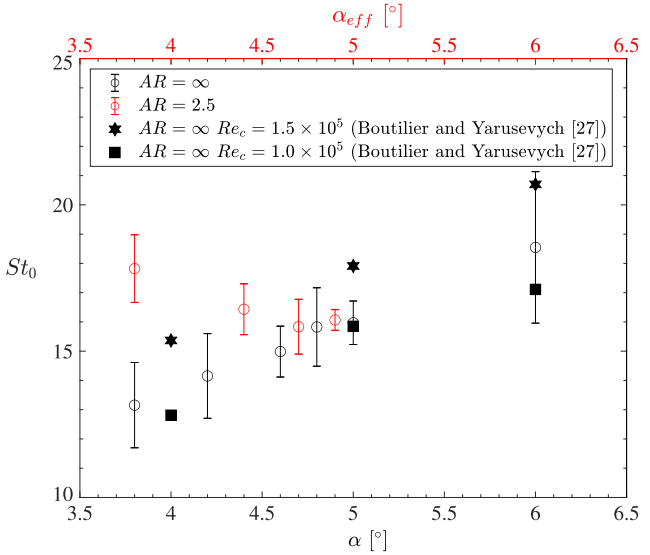

Fig. 16 Central frequency of amplified disturbances for the airfoil and wing at 3.8 deg $\leq \alpha \leq$ 6 deg and $\alpha = 6$ deg, respectively. Data at $Re_c = 1.0 \times 10^5$ and 1.5×10^5 from Ref. [27].

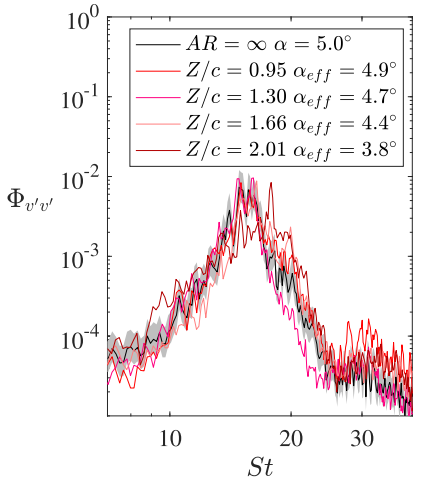

Fig. 17 Surface-normal fluctuating velocity spectra evaluated at $y = \delta^*$ and $\overline{x_t}$ on wing (red) and airfoil (black). Each spectrum has been normalized by its total energy content. Shaded region indicates uncertainty in power spectral density magnitude for the airfoil at $\alpha = 5$ deg.

the wing are similar to that seen for the two-dimensional airfoil at $\alpha = 5.0$ deg, which is expected from the relatively small change in the effective angles of attack from 4.9 to 4.7 deg. Near the wing tip ($Z/c = 2.01$), despite the decrease in effective angle of attack to $\alpha_{\text{eff}} = 3.8$ deg, the most amplified frequency does not shift to lower frequencies. However, a slightly wider band of amplified frequencies is observed. This is attributed to the increased height of the separation bubble at this location, which is expected to lead to a broadening of the unstable frequency range as the inflection point of the separated shear layer moves away from the wall [43].

The top-view PIV measurements provide further insight into the spanwise structure of the shear layer rollup process, with representative instantaneous measurements conducted at an angle of attack of $\alpha = 6.0$ deg for both models presented in Fig. 18. Note that the sampling rate of the top-view measurements is orders of magnitude lower than the relevant time scales of the vortex shedding process, producing measurements of uncorrelated velocity fields. The light sheet for the top-view measurements was positioned to intersect the top halves of the shear layer rollup vortices; as a consequence, the dominant spanwise rollers appear as bands of high streamwise velocity. In agreement with the side-view PIV measurements, the rollup vortices on the wing (Fig. 18b) form further downstream in comparison to the airfoil (Fig. 18a), which is attributed to the lower effective angle of attack. For comparison, the mean locations of separation (solid lines), transition (dashed lines), and reattachment (dotted lines) obtained from side-view measurements are shown in Fig. 18. The results reveal a strongly two-dimensional initial vortex formation process on the airfoil, in agreement with previous studies on LSBs at low levels of freestream turbulence [8,40,47]. Previous investigators have attributed this to the LSB transition being driving by a Kelvin–Helmholtz instability, leading to the preferential amplification of two-dimensional modes [13,48,49]. However, shortly downstream, notable spanwise undulations develop in the spanwise vortex filaments, and three-dimensional breakdown to turbulence occurs downstream of the mean reattachment location, which is evidenced by the appearance of numerous low-velocity "patches" across the span (Fig. 18a). For the wing, a strikingly similar degree of spanwise uniformity is observed in the shear layer rollup vortices (Fig. 18b), along with a similar three-dimensional breakdown to turbulence that occurs downstream of mean reattachment. Furthermore, the rollup vortices on the wing in the range of $0.95 \leq Z/c \leq 2.01$ are not appreciably deformed, indicating that the reduction in local effective angle of attack has little effect on the vortex topology in this region. Incorporating the results of spectral analysis, it can be concluded that spanwise variations in LSB dynamics on a finite wing are not predicated on the local changes of the effective angle of attack. Instead, salient vortex shedding characteristics do not change appreciably over the span of the wing, and they are well approximated by those seen on a two-dimensional airfoil at the same angle of attack as the effective angle of the wing root. It is important to note, however, that more pronounced variations in LSB characteristics may take place in the immediate vicinity of the wing tip.

IV. Conclusions

The effects of the finite aspect ratio on flow development in an LSB have been studied for a semispan wing with an aspect ratio of $AR = 2.5$ at $\alpha = 6$ deg and $Re_c = 1.25 \times 10^5$. Measurements were conducted using surface pressure taps and two-component planar PIV on two-dimensional airfoil and finite wing models, enabling a direct comparison of LSB behavior in flows over two- and three-dimensional geometries. The attention was focused on LSB formation in the region of the wing where spanwise flow velocities were small, but finite-aspect-ratio effects were still present.

Mean pressure measurements revealed a pressure plateau characteristic of an LSB on the suction surfaces of the airfoil and wing. Spanwise pressure measurements were used to quantify the variation of the surface pressure across the span of the wing model. On the basis of a quantitative comparison with streamwise pressure distributions obtained over a relevant range of angles of attack on the airfoil, a methodology for estimating local effective angle of attack was introduced. The results were shown to conform to the lifting line theory predictions, supporting such an approximation for flows over lifting surfaces involving LSBs.

A detailed comparison of PIV measurements conducted on the airfoil and wing was conducted over similar effective angles of attack. Mean flowfield measurements showed that the LSB on the airfoil moved downstream and increased in length as the angle of attack was decreased, in accordance with the trends previously reported in the literature. In contrast, for a similar change in the effective angle of attack, the LSB on the wing remained essentially invariant to the changes in the effective angle of attack across the span of the wing. Its streamwise location and extent closely corresponded to those of an LSB forming on the airfoil at the effective angle of attack of the wing root. Although no substantial changes in LSB location were observed along the span, the LSB on the wing displayed substantial spanwise changes in reverse flow magnitude and displacement thickness when compared to the airfoil.

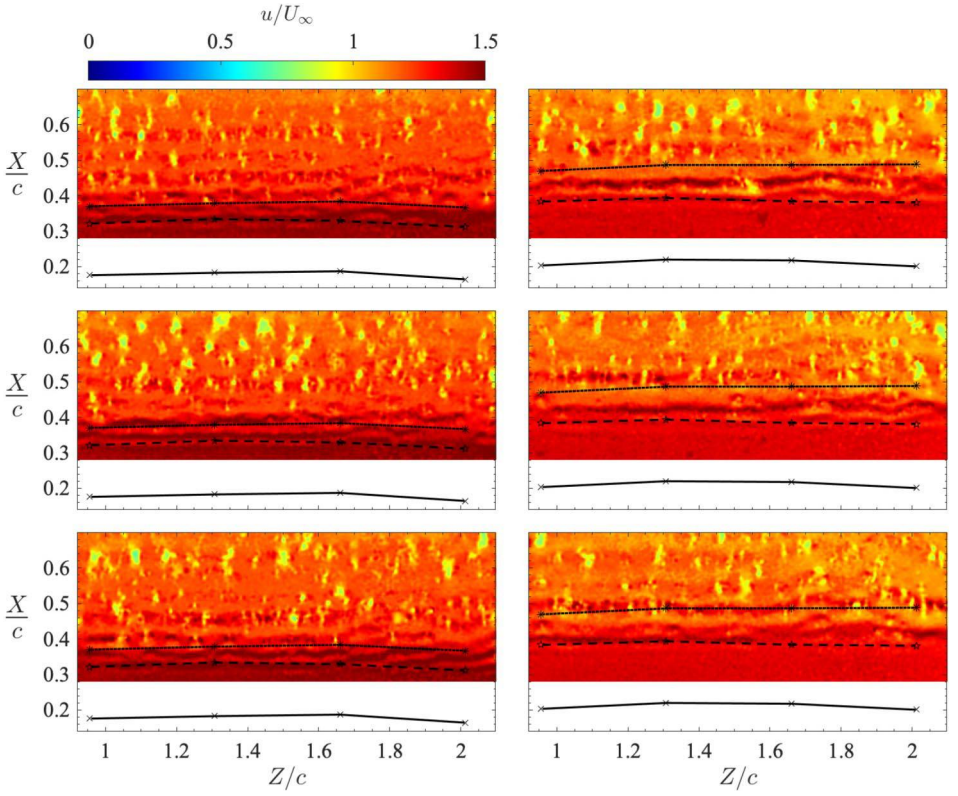

a) Airfoil **b) AR = 2.5 wing**

Fig. 18 Instantaneous streamwise velocity contours: $\alpha = 6$ deg. Solid, dashed, and dotted lines are linear fits to $\overline{x_s}$, $\overline{x_t}$, and $\overline{x_r}$, respectively.

Time-resolved PIV measurements were used to characterize the frequencies of amplified disturbances leading to the formation of dominant spanwise vortices in the separated shear layer. On the airfoil, the central instability frequency decreased as the angle of attack decreased, agreeing with trends previously reported in the literature. In contrast, the central instability frequency on the wing remained unaffected by the change in effective angle of attack along the span, remaining close to that on the airfoil at the angle of attack matching the effective angle at the wing root. The spanwise uniformity in salient LSB dynamics characteristics were further supported by top-view measurements, illustrating strong spanwise uniformity in the shear layer rollers. Thus, the relative spanwise uniformity in mean LSB topology and its dynamics across the wingspan, exuding the regions in the immediate vicinity of the wing tip and root, suggest that the analogy between sectional wing characteristics and airfoil parameters at the same effective angle of attack is not universal in the presence of the LSB. Instead, LSB characteristics obtained on an airfoil at the effective angle of attack of the wing root provide a reasonable approximation for salient LSB characteristics across the wing. It should be noted that these conclusions are not inclusive of the regions in the immediate vicinity of the wing tip/root, which were not considered in the present investigation. Significant three-dimensional effects expected in these regions may cause notable changes in the LSB parameters on finite wings, which is of interest for future investigations.

Acknowledgment

The authors gratefully acknowledge the Natural Sciences and Engineering Research Council of Canada for funding this work. (NSERC Discovery RGPIN-2017-04222).

References

[1] Lissaman, P. B. S., "Low-Reynolds-Number Airfoils," *Annual Review of Fluid Mechanics*, Vol. 15, No. 1, 1983, pp. 223–239. https://doi.org/10.1146/annurev.fl.15.010183.001255

[2] Carmichael, B. H., "Low Reynolds Number Airfoil Survey," NASA CR-165803, Oct. 1981.

[3] Tani, I., "Low-Speed Flows Involving Bubble Separations," *Progress in Aerospace Sciences*, Vol. 5, 1964, pp. 70–103. https://doi.org/10.1016/0376-0421(64)90004-1

[4] Dovgal, A., Kozlov, V., and Michalke, A., "Laminar Boundary Layer Separation: Instability and Associated Phenomena," *Progress in Aerospace Sciences*, Vol. 30, No. 1, 1994, pp. 61–94. https://doi.org/10.1016/0376-0421(94)90003-5

[5] Boutilier, M. S. H., and Yarusevych, S., "Separated Shear Layer Transition over an Airfoil at a Low Reynolds Number," *Physics of Fluids*, Vol. 24, No. 8, 2012, Paper 084105. https://doi.org/10.1063/1.4744989

[6] Burgmann, S., Dannemann, J., and Schröder, W., "Time-Resolved and Volumetric PIV Measurements of a Transitional Separation Bubble on an SD7003 Airfoil," *Experiments in Fluids*, Vol. 44, No. 4, 2008, pp. 609–622. https://doi.org/10.1007/s00348-007-0421-0

[7] Yarusevych, S., Sullivan, P. E., and Kawall, J. G., "On Vortex Shedding from an Airfoil in Low-Reynolds-Number Flows," *Journal of Fluid Mechanics*, Vol. 632, Aug. 2009, pp. 245–271. https://doi.org/10.1017/S0022112009007058

[8] Kurelek, J. W., Lambert, A. R., and Yarusevych, S., "Coherent Structures in the Transition Process of a Laminar Separation Bubble," *AIAA Journal*, Vol. 54, No. 8, 2016, pp. 2295–2309. https://doi.org/10.2514/1.J054820

[9] Horton, H. P., "Laminar Separation Bubbles in Two and Three Dimensional Incompressible Flow," Ph.D. Thesis, Univ. of London, London, 1968.

[10] Gaster, M., "The Structure and Behaviour of Laminar Separation Bubbles," Aeronautical Research Council R&M 3595, London, 1967.

[11] O'Meara, M. M., and Mueller, T. J., "Laminar Separation Bubble Characteristics on an Airfoil at Low Reynolds Numbers," *AIAA Journal*, Vol. 25, No. 8, 1987, pp. 1033–1041. https://doi.org/10.2514/3.9739

[12] Alam, M., and Sandham, N. D., "Direct Numerical Simulation of 'Short' Laminar Separation Bubbles with Turbulent Reattachment," *Journal of Fluid Mechanics*, Vol. 410, May 2000, pp. 1–28. https://doi.org/10.1017/S0022112099008976

[13] Diwan, S. S., and Ramesh, O. N., "On the Origin of the Inflectional Instability of a Laminar Separation Bubble," *Journal of Fluid Mechanics*,

Vol. 629, June 2009, pp. 263–298.
https://doi.org/10.1017/S002211200900634X
[14] Marxen, O., Lang, M., and Rist, U., "Vortex Formation and Vortex Breakup in a Laminar Separation Bubble," *Journal of Fluid Mechanics*, Vol. 728, Aug. 2013, pp. 58–90.
https://doi.org/10.1017/jfm.2013.222
[15] Torres, G. E., and Mueller, T. J., "Low Aspect Ratio Aerodynamics at Low Reynolds Numbers," *AIAA Journal*, Vol. 42, No. 5, 2004, pp. 865–873.
https://doi.org/10.2514/1.439
[16] Shields, M., and Mohseni, K., "Effects of Sideslip on the Aerodynamics of Low-Aspect-Ratio Low-Reynolds-Number Wings," *AIAA Journal*, Vol. 50, No. 1, 2012, pp. 85–99.
https://doi.org/10.2514/1.J051151
[17] Chen, Z. J., Qin, N., and Nowakowski, A. F., "Three-Dimensional Laminar-Separation Bubble on a Cambered Thin Wing at Low Reynolds Numbers," *Journal of Aircraft*, Vol. 50, No. 1, 2013, pp. 152–163.
https://doi.org/10.2514/1.C031829
[18] Ananda, G. K., Sukumar, P. P., and Selig, M. S., "Measured Aerodynamic Characteristics of Wings at Low Reynolds Numbers," *Aerospace Science and Technology*, Vol. 42, April 2015, pp. 392–406.
https://doi.org/10.1016/j.ast.2014.11.016
[19] Genç, M. S., Özkan, G., Özden, M., Ki˙ri˙ş, M. S., and Yi˙ldi˙z, R., "Interaction of Tip Vortex and Laminar Separation Bubble over Wings with Different Aspect Ratios Under Low Reynolds Numbers," *Journal of Mechanical Engineering Science*, Vol. 232, No. 22, 2018, pp. 4019–4037.
https://doi.org/10.1177/0954406217749270
[20] Herbst, S. L., Hain, R., and Kähler, C. J., *Low Aspect Ratio Wing Under Large-Scale Turbulent Inflow Conditions at Low Reynolds Numbers*, Vol. 142, Notes on Numerical Fluid Mechanics and Multidisciplinary Design, Springer-Verlag, New York, 2020, pp. 653–662.
https://doi.org/10.1007/978-3-030-25253-3_62
[21] McMasters, J. H., and Henderson, M. L., "Low-Speed Single-Element Airfoil Synthesis," *Technical Soaring*, Vol. 6, No. 2, 1980, pp. 1–21.
[22] Mueller, T. J., and DeLaurier, J. D., "Aerodynamics of Small Vehicles," *Annual Review of Fluid Mechanics*, Vol. 35, Jan. 2003, pp. 89–111.
https://doi.org/10.1146/annurev.fluid.35.101101.161102
[23] Awasthi, M., Moreau, D., and Doolan, C., "Flow Structure of a Low Aspect Ratio Wall-Mounted Airfoil Operating in a Low Reynolds Number Flow," *Experimental Thermal and Fluid Science*, Vol. 99, Dec. 2018, pp. 94–116.
https://doi.org/10.1016/j.expthermflusci.2018.07.019
[24] Marchman, J. F., and Abtahi, A., "Aerodynamics of an Aspect Ratio 8 Wing at Low Reynolds Numbers," *Journal of Aircraft*, Vol. 22, No. 7, 1985, pp. 628–634.
https://doi.org/10.2514/3.45176
[25] Applin, Z. T., "Pressure Distributions from Subsonic Tests of a NACA 0012 Semispan Wing Model," NASA TM-110148, Sept. 1995.
[26] Prandtl, L., "Applications of Modern Hydrodynamics to Aeronautics," NACA TR-116, Dec. 1922.
[27] Boutilier, M. S. H., and Yarusevych, S., "Parametric Study of Separation and Transition Characteristics over an Airfoil at Low Reynolds Numbers," *Experiments in Fluids*, Vol. 52, No. 6, 2012, pp. 1491–1506.
https://doi.org/10.1007/s00348-012-1270-z
[28] Bastedo, W. G., and Mueller, T. J., "Spanwise Variation of Laminar Separation Bubbles on Wings at Low Reynolds Number," *Journal of Aircraft*, Vol. 23, No. 9, 1986, pp. 687–694.
https://doi.org/10.2514/3.45363
[29] Demir, H., Özden, M., Genç, M. S., and Çağdaş, M., "Numerical Investigation of Flow on NACA4412 Aerofoil with Different Aspect Ratios," *EPJ Web of Conferences*, Vol. 114, March 2016, Paper 02016.
https://doi.org/10.1051/epjconf/201611402016
[30] Garmann, D. J., and Visbal, M. R., "Analysis of Tip Vortex Near-Wake Evolution for Stationary and Oscillating Wings," *AIAA Journal*, Vol. 55, No. 8, 2017, pp. 2686–2702.
https://doi.org/10.2514/1.J055574
[31] Huang, R. F., and Lin, C. L., "Vortex Shedding and Shear-Layer Instability of Wing at Low-Reynolds Numbers," *AIAA Journal*, Vol. 33, No. 8, 1995, pp. 1398–1403.
https://doi.org/10.2514/3.12561
[32] Scarano, F., and Riethmuller, M. L., "Advances in Iterative Multigrid PIV Image Processing," *Experiments in Fluids*, Vol. 29, No. 7, 2000, pp. S051–S060.
https://doi.org/10.1007/s003480070007
[33] Westerweel, J., "Efficient Detection of Spurious Vectors in Particle Image Velocimetry Data," *Experiments in Fluids*, Vol. 16, Nos. 3–4, 1994, pp. 236–247.
https://doi.org/10.1007/BF00206543
[34] Welch, P., "The Use of Fast Fourier Transform for the Estimation of Power Spectra: A Method Based on Time Averaging over Short, Modified Periodograms," *IEEE Transactions on Audio and Electroacoustics*, Vol. 15, No. 2, 1967, pp. 70–73.
https://doi.org/10.1109/TAU.1967.1161901
[35] Manolakis, D., Ingle, V., and Kagon, S., "Nonparametric Power Spectrum Estimation," *Statistical and Adaptive Signal Processing*, McGraw–Hill, Boston, 2000, Chap. 5.
[36] Wieneke, B., "PIV Uncertainty Quantification from Correlation Statistics," *Measurement Science and Technology*, Vol. 26, No. 7, 2015, Paper 074002.
https://doi.org/10.1088/0957-0233/26/7/074002
[37] Moffat, R. J., "Describing the Uncertainties in Experimental Results," *Experimental Thermal and Fluid Science*, Vol. 1, No. 1, 1988, pp. 3–17.
https://doi.org/10.1016/0894-1777(88)90043-X
[38] Gudmundsson, S., "The Anatomy of the Wing," *General Aviation Aircraft Design*, Elsevier, New York, 2014, pp. 299–399, Chap. 9.
https://doi.org/10.1016/B978-0-12-397308-5.00009-X
[39] Theodoresen, T., "The Theory of Wind-Tunnel Wall Interference," NACA TR-410, Dec. 1931.
[40] Kirk, T. M., and Yarusevych, S., "Vortex Shedding Within Laminar Separation Bubbles Forming over an Airfoil," *Experiments in Fluids*, Vol. 58, No. 5, 2017, Paper 43.
https://doi.org/10.1007/s00348-017-2308-z
[41] Hain, R., Kähler, C. J., and Radespiel, R., "Dynamics of Laminar Separation Bubbles at Low-Reynolds-Number Aerofoils," *Journal of Fluid Mechanics*, Vol. 630, July 2009, pp. 129–153.
https://doi.org/10.1017/S0022112009006661
[42] Wu, J. Z., Tramel, R. W., Zhu, F. L., and Yin, X. Y., "A Vorticity Dynamics Theory of Three-Dimensional Flow Separation," *Physics of Fluids*, Vol. 12, No. 8, 2000, pp. 1932–1954.
https://doi.org/10.1063/1.870442
[43] Michalke, A., "On the Inviscid Instability of Wall-Bounded Velocity Profiles Close to Separation," *Separated Flows and Jets*, edited by V. V. Kozlov, and A. V. Dovgal, Springer-Verlag, Berlin, 1991, pp. 557–564.
https://doi.org/10.1007/978-3-642-84447-8_74
[44] Yarusevych, S., and Kotsonis, M., "Steady and Transient Response of a Laminar Separation Bubble to Controlled Disturbances," *Journal of Fluid Mechanics*, Vol. 813, Feb. 2017, pp. 955–990.
https://doi.org/10.1017/jfm.2016.848
[45] Rodríguez, D., and Theofilis, V., "Structural Changes of Laminar Separation Bubbles Induced by Global Linear Instability," *Journal of Fluid Mechanics*, Vol. 655, July 2010, pp. 280–305.
https://doi.org/10.1017/S0022112010000856
[46] Häggmark, C. P., Bakchinov, A. A., and Alfredsson, P. H., "Experiments on a Two-Dimensional Laminar Separation Bubble," *Philosophical Transactions of the Royal Society of London, Series A: Mathematical, Physical and Engineering Sciences*, Vol. 358, No. 1777, 2000, pp. 3193–3205.
https://doi.org/10.1098/rsta.2000.0704
[47] Nati, A., de Kat, R., Scarano, F., and van Oudheusden, B. W., "Dynamic Pitching Effect on a Laminar Separation Bubble," *Experiments in Fluids*, Vol. 56, No. 9, 2015, Paper 172.
https://doi.org/10.1007/s00348-015-2031-6
[48] Marxen, O., Lang, M., and Rist, U., "Discrete Linear Local Eigenmodes in a Separating Laminar Boundary Layer," *Journal of Fluid Mechanics*, Vol. 711, Nov. 2012, pp. 1–26.
https://doi.org/10.1017/jfm.2012.263
[49] Squire, H. B., "On the Stability for Three-Dimensional Disturbances of Viscous Fluid Flow Between Parallel Walls," *Proceedings of the Royal Society of London. Series A: Containing Papers of a Mathematical and Physical Character*, Vol. 142, No. 847, 1933, pp. 621–628.
https://doi.org/10.1098/rspa.1933.0193

F. N. Coton
Associate Editor